water

MDPI

Article

Diethylene Glycol-Assisted Organized TiO_2 Nanostructures for Photocatalytic Wastewater Treatment Ceramic Membranes

Rizwan Ahmad [1,2,†], Jin Kyu Kim [3,†], Jong Hak Kim [3,*] and Jeonghwan Kim [1,*]

1 Department of Environmental Engineering, Inha University, Inharo-100, Michuholgu, Incheon 22212, Korea; rahmad@cuilahore.edu.pk
2 Department of Chemical Engineering, COMSATS University Islamabad (CUI), Lahore Campus, Defense Road, Off Raiwind Road, Lahore 45550, Pakistan
3 Department of Chemical and Biochemical Engineering, Yonsei University, 50 Yonsei-ro, Seodaemun-gu, Seoul 03722, Korea; jkk4885@gmail.com
* Correspondence: jonghak@yonsei.ac.kr (J.H.K.); jeonghwankim@inha.ac.kr (J.K.); Tel.: +82-32-860-7502 (J.K.)
† These authors contributed equally to this work.

Received: 16 March 2019; Accepted: 6 April 2019; Published: 10 April 2019

Abstract: A high-performance photocatalytic ceramic membrane was developed by direct growth of a TiO_2 structure on a macroporous alumina support using a hydrothermal method. The morphological nanostructure of TiO_2 on the support was successfully controlled via the interaction between the TiO_2 precursor and a capping agent, diethylene glycol (DEG). The growth of anatase TiO_2 nanorods was observed both on the membrane surface and pore walls. The well-organized nanorods TiO_2 reduced the perturbation of the alumina support, thus controlling the hydrolysis rate of the TiO_2 precursor and reducing membrane fouling. However, a decrease in the amount of the DEG capping agent significantly reduced membrane permeability, owing to the formation of nonporous clusters of TiO_2 on the support. Distribution of the organized TiO_2 nanorods on the support was very effective for the improvement of the organic removal efficiency and antifouling under ultraviolet illumination. The TiO_2 nanostructure associated with the reactive crystalline phase, rather than the amount of layered TiO_2 formed on the support, which was found to be the key to controlling photocatalytic membrane reactivity. These experimental findings would provide a new approach for the development of efficacious photocatalytic membranes with improved performance for wastewater treatment.

Keywords: diethylene glycol; photocatalytic membrane; antifouling; photodegradation; nanostructure

1. Introduction

Membranes are effective tools for the removal of various contaminants from water sources. As opposed to conventional treatments, membrane processes afford excellent water quality (permeate) and reduce operational costs because of the minimal chemical demands and small footprint [1–5]. Nevertheless, membrane filtration is always hindered by the phenomenon of membrane fouling caused by the deposition of contaminants, resulting in pore blockage and cake layer formation on the membrane. Membrane fouling lowers membrane permeability, thus necessitating chemical cleaning and shortens the membrane's lifetime [6–8].

Ceramic membranes have many advantages over polymeric membranes, including longer service life, superior thermal and chemical resistance, and better fouling resistance, owing to their hydrophilic surface with a low contact angle [9–13]. Recent advances in membrane fabrication techniques have enabled the development of ceramic membranes with higher reactivities and widespread applications beyond their traditional role as a separation tool. Ceramic membranes are also valuable for the

treatment of high-strength wastewater, such as industrial wastewater, where polymeric membranes are not suitable.

There is rapidly growing interest in the development of self-cleaning ceramic membranes and their application in water treatments targeting organic contaminants. Membrane performance can be improved by increasing the catalytic membrane surface area and permeability, for example, by the removal of the target contaminants concentrated on the membrane [14,15]. Ceramic membranes have a catalytic layer consisting of catalytic nanoparticles such as iron oxide, which can enhance the decomposition of natural organic matter as it is combined with chemical oxidation promoters such as ozonation [16]. Ceramic alumina (Al_2O_3) membranes have been modified by coating with titanium dioxide (TiO_2) nanoparticles to improve membrane permeability and surface reactivity by removing both organic pollutants and membrane fouling under direct ultraviolet (UV) irradiation on the membrane surface [17,18]. TiO_2 has been extensively used for the development of catalytic films due to its wide band gap (anatase: E_g = 3.2 eV), low toxicity, low cost, chemical stability and high photocatalytic activity [19,20]. For improved catalytic efficiency, the controlled immobilization of the TiO_2 nanostructure is necessary [21,22].

Catalytic sites with well-controlled structures form the core of a self-cleaning ceramic membrane filtration [23,24]. Improved antifouling was demonstrated with a photocatalytic ceramic membrane consisting of an organized mesoporous TiO_2 layer on a porous alumina support [23,25,26]. A series of photocatalytic TiO_2 membranes were developed on the macroporous support by the sol-gel route using polymer templates [27]. Precoating of poly (vinyl pyrrolidone) (PVP) homopolymer as the sacrificing agent inside the membrane pores proved an effective way for generating a well-organized TiO_2 mesostructure and improved the performance owing to the minimized pore infiltration of the precursor/polymer template solutions. Nevertheless, perturbation of the membrane support by catalyst films produced through the sol-gel route is a serious challenge [28]. The efficient growth of nanostructured TiO_2 on a support with high porosity and catalytic activity is the key to developing efficacious photocatalytic membranes. However, most previous studies for photocatalytic degradation were investigated in a batch mode without considering the self-cleaning efficiency of the membrane during membrane filtration [29]. Little information is available in the literature regarding the significance of catalyst distribution and crystalline structure on membrane surfaces or within pore walls to enhance membrane reactivity.

In this paper, we described a high-performance photocatalytic membrane based on diethylene glycol (DEG)-assisted TiO_2 nanostructure on a porous alumina support for wastewater treatment. A hydrothermal method was used to enable the direct growth of well-controlled TiO_2 structures on the membrane without precoating with a sacrificing agent (e.g., PVP), which would otherwise be required to prevent structure collapse. TiO_2 nanostructures with different morphologies on the support were produced by interactions between the TiO_2 precursor and a capping agent, i.e., DEG. DEG was utilized to retard the hydrolysis of potassium titanium oxide oxalate dehydrate (PTO) for elaborate control of the TiO_2 nanostructure. The antifouling properties of the membrane and degradation of organic compounds through membrane filtration were also evaluated in the photocatalytic membrane reactor especially designed for this study.

2. Materials and Methods

2.1. Materials

Potassium titanium oxide oxalate dehydrate (PTO, Molecular Weight (M_W): 354 g mol^{-1}) and DEG (M_W: 106 g mol^{-1}) were purchased from Sigma-Aldrich (St. Louis, MO, USA) and used without any further treatment. The alumina support (α-Al_2O_3, pore size = 100 nm, diameter = 30 mm, thickness = 2 mm) was purchased from Nano Pore Materials Co., Ltd (Albuquerque, NM, USA).

2.2. DEG-Assisted Synthesis of TiO_2 Nanostructure

To prepare the TiO_2 precursor solution, 0.73 g of PTO was completely dissolved in deionized water by magnetic stirring, after which DEG was added to the solution dropwise. The resulting mixture was stirred for more than 30 min to induce interaction between the TiO_2 precursor and the solvents. For the control of TiO_2 nanostructures on the alumina support, the ratio of water to DEG was set to 9:31, 11:29, or 13:27 with a fixed total volume of 40 mL of solvent. The resulting structures were denoted T1, T2, and T3, respectively. The well-mixed TiO_2 precursor solution was poured into a Teflon-lined autoclave with a bare alumina membrane leaning against the wall. The autoclave was kept at 200 °C for 11 h in an oven and then cooled naturally. The TiO_2 nanostructures grown on the alumina support were taken out of the solution and washed with ethanol and water to remove the residual TiO_2 precursor and organics from the membrane. The membranes were completely dried in an oven and calcined at 500 °C for 1 h to crystallize the TiO_2 structures and remove residual organic materials.

2.3. Membrane Characterization

Surfaces and cross-sections of the TiO_2 structures on the support were characterized by field emission scanning electron microscopy (FE-SEM, JEOL-7800F, JEOL Ltd., Tokyo, Japan). The crystalline phases of the TiO_2 structures on the support were investigated with X-ray diffraction spectroscopy (XRD) (D8 ADVANCE with DAVINCI, BRUKER, Hamburg, Germany, 40 kV, 40 mA, wavelength (λ): Cu kα1-1.5418 Å). Three-dimensional surface structures of TiO_2 on the support were analyzed with atomic force microscopy (AFM, XE-Bio, Park Systems, Suwon, Korea).

The overall porosity of each membrane was estimated using Equation (1) [25,30]:

$$\varepsilon = \frac{w_1 - w_2}{A\,L\,\rho_w} \tag{1}$$

where w_1 and w_2 represent the weight (g) of the wet and dry membrane, respectively, A is the effective membrane area (cm^2), ρ_w is the density of pure water (g cm^{-3}), and L is the membrane thickness (cm) measured by a digital micrometer (Mitutoyo, MDC-25PX, Kawasaki, Japan).

2.4. Photocatalytic Membrane Reactor

Figure 1 illustrates the laboratory-scale photocatalytic membrane reactor used in this study. A photocatalytic batch reactor using a jacketed beaker was used to evaluate the adsorption capacity and surface photocatalytic activity of the membrane, as shown in Figure 1a. A 300 W UVA lamp (Osram Ultra-Vitalux, Munich, Germany) with 365 nm wavelength was positioned above a beaker containing a test solution consisting of Congo Red dye (formula: $C_{32}H_{22}N_6Na_2O_6S_2$, molecular weight: 697 g $mole^{-1}$). The concentration of Congo Red dye was 5 mg L^{-1}. Tap water was recirculated through the reactor using a chiller (Jeio Tech Co., Daejeon, South Korea). First, the membrane was immersed in a 50 mL of feed solution without UV irradiation. After that, the membrane was exposed to continuous stirring for 3 h to ensure contact of the organic materials with the membrane and to achieve adsorption equilibrium. Both stirrer and membrane were placed at the corners of the jacketed beaker and kept at a sufficient distance to avoid any physical contact. The same experiments were conducted with UV irradiation of the membrane surface for comparison. Sample aliquots were withdrawn at regular time intervals to measure the concentrations of Congo Red dye using a UV-Vis spectrometer (Thermo Fischer Scientific, Waltham, MA, USA) at 496 nm wavelength. After the analysis, the samples were returned to the reactor. Blank experiments were also performed using a bare support membrane to investigate the effect of photolysis on the degradation of organic dye. Removal efficiency by adsorption for each membrane was estimated using Equation (2):

$$\text{Adsorption}\ (\%) = \frac{\left(C_0 - C_{eq}\right)}{C_0} \times 100 \tag{2}$$

where C_0 and C_{eq} are the feed concentration and the concentration of Congo Red dye after 3 h, respectively. In this study, the 3 h operational time was needed to obtain higher than 90% removal efficiency of Congo Red dye in photocatalytic membrane reactor.

To perform membrane filtration, a laboratory-scale cross-flow filtration setup was developed, as shown in Figure 1b. A circular type of cross-flow membrane module was made from stainless steel, with a quartz window to allow UV light to be transmitted directly onto the membrane surface. The effective surface area of the membrane was 5.3 cm^2. A 300 W UVA lamp with a wavelength of 365 nm was positioned about 5 cm from the quartz window above the membrane surface. A compressed oxygen gas tank was connected to the pressurized vessel containing a feed solution. A pressure of 1.5 bar was applied to the membrane module, which was connected to the vessel. The cross-flow rate was maintained by recirculating a feed solution at 0.4 L min^{-1} through a recirculation pump. UV on-off tests were performed to better understand membrane reactivity and permeate flux recovery under UV irradiation. A feed solution of 10 mg L^{-1} of Congo Red dye was used for membrane filtration. The filtration cycle was based on 1 h filtration without UV irradiation followed by 1 h filtration with UV irradiation, with a total filtration time of 4 h. The permeate from the membrane was collected in the permeate reservoir, which was positioned on an electric balance connected to the data acquisition system to record the increase in permeate weight with time. Experiments were performed three times and an average value was taken under each operational condition.

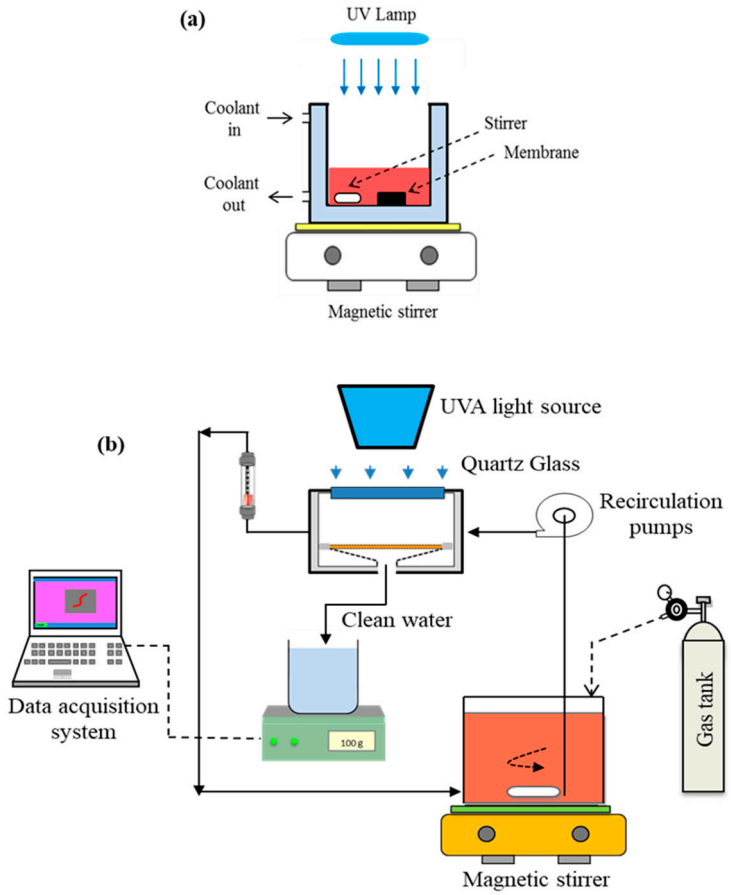

Figure 1. (**a**) Experimental setup for investigating photocatalytic activity of membranes in the batch test, (**b**) experimental setup for the photocatalytic membrane reactor (PMR).

3. Results

3.1. DEG-Assistend Synthesis of TiO_2 Nanostrtuctures

To synthesize various TiO_2 nanostructures on the support, PTO and DEG were utilized as the TiO_2 precursor and capping agent, respectively. The capping agent is integral to the formation of structures and therefore should be carefully selected to ensure structure control [31,32]. DEG is known to be effective for adjusting the hydrolysis rate of the precursor during structure formation, enabling precise control of the resulting structures. As a capping agent, it retards the hydrolysis rate of PTO, resulting in the directional growth of TiO_2 structures [33,34]. Therefore, the volume ratio of water to DEG applied for the hydrothermal synthesis was considered the key parameter to control the TiO_2 nanostructures directly grown on the support.

The surfaces of the TiO_2 nanostructures on the support were characterized with FE-SEM (Figure 2). As shown in Figure 2a,b, the bare alumina membrane as a macroporous support (average pore size = 100 nm) was composed of large Al_2O_3 particles with an irregular size and shape. The hydrothermal reaction resulted in the formation of TiO_2 nanorods directly grown on the surface of the support. In contrast to sol-gel coated membranes, the porous structure of the support membrane was not significantly perturbed by the growth of the TiO_2 nanorod structures (in the case of T1). This indicated that the TiO_2 nanostructure might not have functioned as the high resistance to mass transport, which could have facilitated high permeate flux of the membrane [25].

As shown in Figure 2e,f, a larger number of TiO_2 nanorods were grown on the surface of the T2 membrane, potentially leading to a reduced water flux in the membrane. The high-density nanorods were somewhat aggregated and shorter than those of T1 owing to the promoted growth of TiO_2 structures. Such a thick layer on the membrane may cause resistance to membrane flow and reduce membrane permeability [25]. However, increased deposition of TiO_2 on the membrane may conversely enhance the membrane permeability because the abundant hydroxyl groups of TiO_2 increase the membrane hydrophilicity under UV illumination [35,36]. Thus, the growth of more TiO_2 nanostructures on the support membrane may be either advantageous or disadvantageous for membrane permeability; this is discussed in the next section.

The thickly formed T3 layer seemed to cause relatively more blocking of the macroporous surface of the support membrane, as shown in Figure 2g,h. The short and thick nanorods clustered together and formed layered structures on the support membrane, potentially lowering the membrane permeability. Low-magnified images of T2 and T3 revealed that their membrane surfaces were covered by TiO_2 structures, leading to a significantly altered surface morphology in comparison with T1 and the bare support membrane. The morphological differences among the membrane surfaces resulted from the differing degrees of TiO_2 growth, based on different interactions between the TiO_2 precursor and capping agent. DEG suppressed the hydrolysis of PTO in a concentration-dependent manner, determining the interactions that take place and thereby the nanostructure morphology. The directional growth of nanorod structures could thus be accelerated by increasing the amount of DEG as a proportion of the total solvent volume. As the amount of DEG decreased, the length of the nanorods decreased and more of the TiO_2 nanostructure was synthesized on the membrane. Accordingly, the nanostructure prepared with the lowest amount of DEG had a layered rather than a nanorod structure (T3 membrane). Therefore, the amount of DEG present during the hydrothermal reaction was the key parameter for controlling the TiO_2 structures on the membranes.

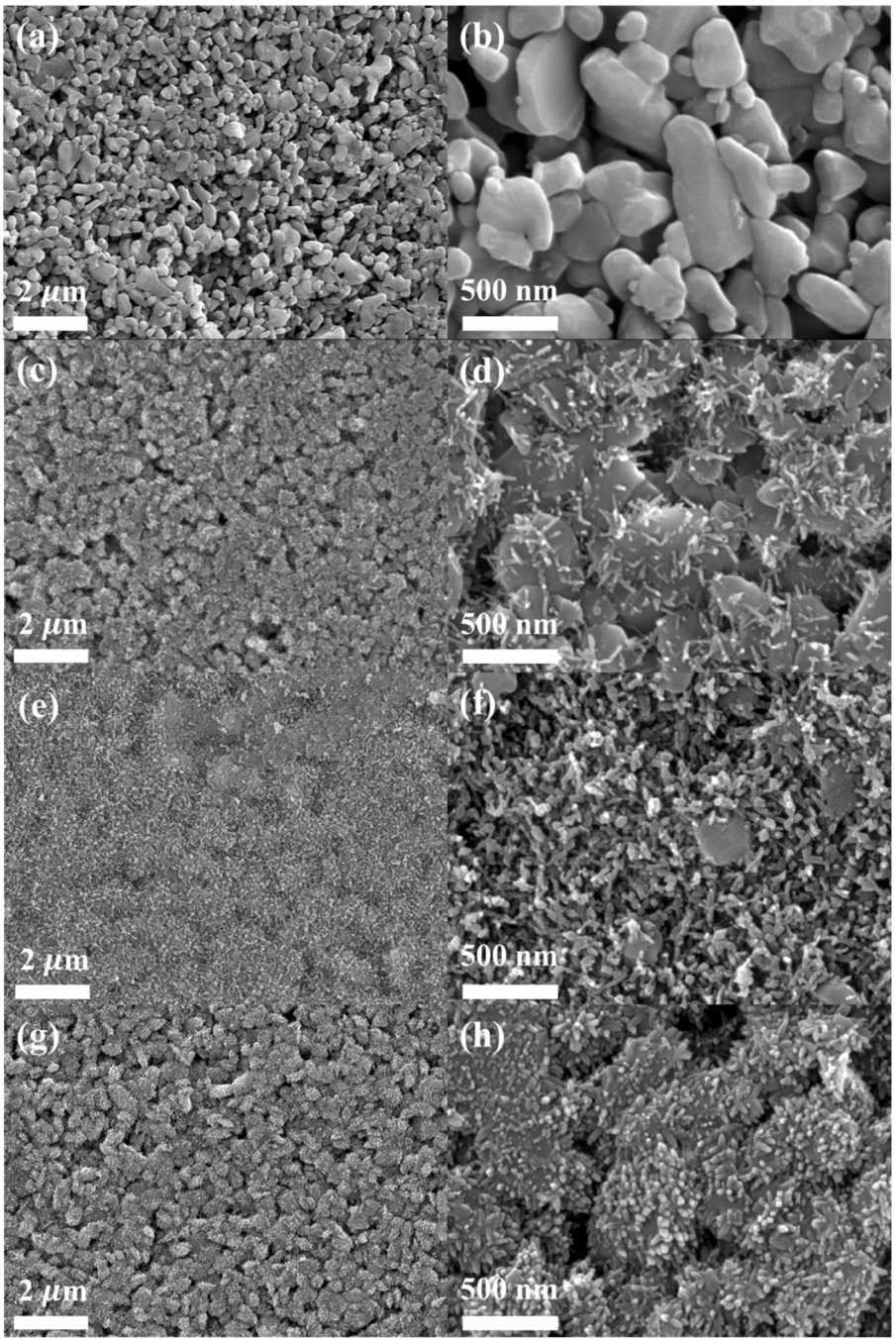

Figure 2. Surface SEM images of (**a**,**b**) the bare alumina support membrane, (**c**,**d**) T1, (**e**,**f**) T2, and (**g**,**h**) T3.

The distribution of TiO_2 nanostructures on the membrane surface was investigated with energy dispersive X-ray spectroscopy (EDS), as shown in Figure 3. Aggregated photocatalysts can cause severe deterioration of photocatalytic activity owing to the decreased number of active sites available for photocatalysis, and uniformly dispersed photocatalysts are essential for the enhancement of photocatalytic activity. Therefore, nonhomogeneous distribution of TiO_2 on a membrane can greatly degrade its photocatalytic performance. The Ti elemental mapping images clearly demonstrated that TiO_2 was homogeneously distributed across the entire membrane surface, for all the membrane types prepared with the different DEG amounts. The atomic percentage (At %) of the Ti element was inversely proportional to the amount of DEG used: T1 (1.21 At %) < T2 (4.36 At %) < T3 (7.84 At %). This trend in the atomic percentage, i.e., the amount of TiO_2, arose because smaller amounts of DEG

facilitated TiO_2 growth on the membrane, as observed in the surface SEM images. In conclusion, TiO_2 structures synthesized based on different interactions between the capping agent and TiO_2 precursor and were uniformly deposited on the support membrane.

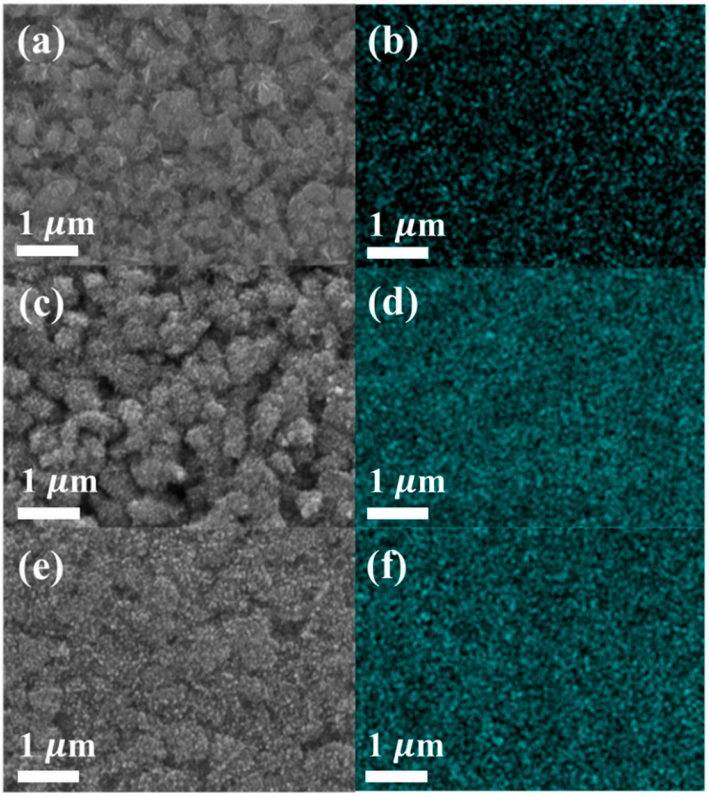

Figure 3. Surface SEM images of (**a**) T1, (**c**) T2, and (**e**) T3. The corresponding EDS elemental (Ti) mapping images of (**b**) T1, (**d**) T2, and (**f**) T3.

The cross-sectional and surface morphologies of TiO_2 structures are strongly related to membrane performance. Cross-sectional images of the TiO_2 nanostructure grown on the support were obtained with SEM (Figure 4). The bare support consisted of a large number of Al_2O_3 macrocrystals, as shown in Figure 4a. In accordance with the surface SEM results, the cross-section of T1 showed deposition of TiO_2 nanorods, as shown in Figure 4b. The nanorods were uniformly grown across the whole cross-section of the membrane. In the cross-section of T2, shown in Figure 4c, aggregated nanorods with high density were observed on the large Al_2O_3 particles, which was consistent with the surface SEM results. The images of T3, shown in Figure 4d, clearly showed that a larger amount of TiO_2 was deposited on the cross-section as well as the surface of the membrane. Based on the cross-section images, T3 appeared to have reduced porosity and less porous structure available for permeation of feed solution in comparison with T1. Such a reduction in the porosity available for permeation not only severely reduces the membrane flux, but also prevents UV light from approaching TiO_2 and might thereby result in the increase of membrane fouling [25]. Therefore, the porosity and porous structure in the membrane cross-section seems to be a pivotal parameter in determining the performance of a photocatalytic membrane and should be considered in order to achieve efficient photocatalysis.

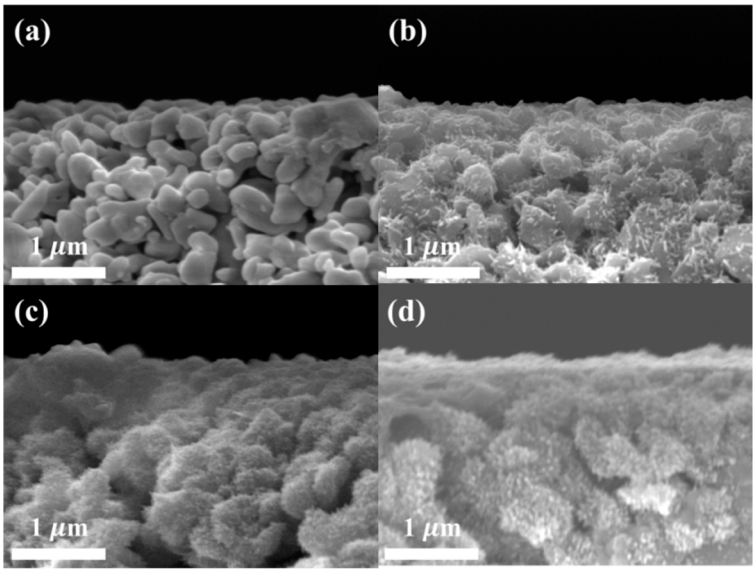

Figure 4. Cross sectional SEM images of the (**a**) bare alumina support, (**b**) T1, (**c**) T2, and (**d**) T3.

The distribution of TiO_2 in the membrane cross-section was also analyzed with EDS, as shown in Figure 5. Smaller amounts of DEG incorporated during the hydrothermal synthesis process promoted the growth of TiO_2, leading to the formation of more extensive TiO_2 layers on the support: T1 (0.32 At %) < T2 (1.92 At %) < T3 (3.12 At %). These results were consistent with the previously discussed Ti elemental distributions on the membrane surface (Figure 3).

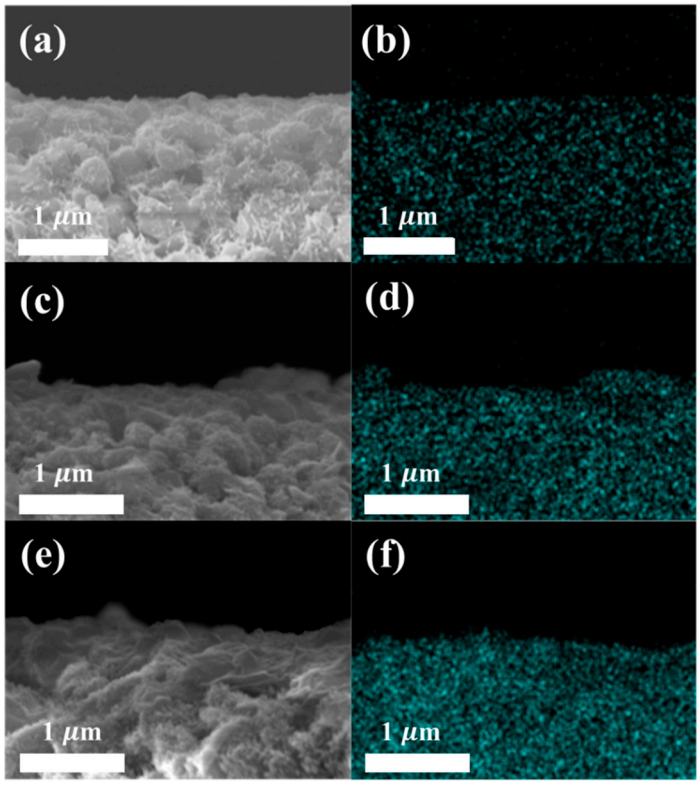

Figure 5. Cross sectional SEM images of (**a**) T1, (**c**) T2, and (**e**) T3. The corresponding EDS elemental (Ti) mapping images of (**b**) T1, (**d**) T2, and (**f**) T3.

The effect of the amount of DEG used on the crystalline property of TiO_2 structures was also investigated by XRD, as shown in Figure 6. The TiO_2 phase was a decisive factor for photocatalytic

activity; the anatase phase was considered more effective in this regard than other phases such as the rutile and brookite phases [37,38]. The higher photocatalytic activity was attributed to the larger surface area, lower recombination rate, and higher electron lifetime of the anatase phase. The bare alumina support exhibited sharp peaks resulting from the highly crystalline α-phase of Al_2O_3 (Joint Committee on Powder Diffraction Standards, JCPDS Card No. 10-0173). In the diffraction pattern of T1, which was synthesized using the largest amount of DEG, the peaks appeared at 2θ = 25.6, 37.8, and 61.3°, corresponding to the (101), (004), and (115) planes of the anatase TiO_2 phase (JCPDS Card No. 21-1272), which is generally considered the most effective phase. The use of smaller amounts of DEG resulted in TiO_2 structures consisting of different phases. The peaks of T2 and T3 at 2θ = 25.6, 37.8, and 61.3° indicated the anatase phase, whereas those at 2θ = 27.4, 36.2, 41.3, and 54.2° represented the (110), (101), (111), and (211) planes of the rutile phase (JCPDS Card No. 21-1276). These differences in the TiO_2 crystalline phases, depending on the DEG amount, resulted from the different interactions between the TiO_2 precursor and DEG. Increasing the amount of DEG used as a capping agent suppressed the formation of the rutile phase, which is unfavorable for photocatalysis of organic materials [33]. Accordingly, T1, which consisted of the pure anatase phase, was expected to exhibit superior photocatalytic activity; refer to the following section on photocatalytic membrane performance.

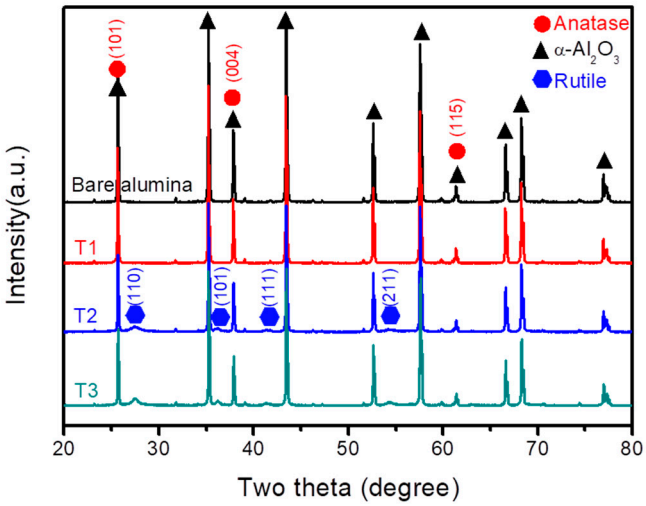

Figure 6. XRD patterns of various membranes.

The three-dimensional surface morphologies of the bare alumina support and the TiO_2 nanostructure grown on the support were characterized by AFM. The surface structures of various membranes are shown in Figure 7; the obtained root-mean-squared roughness (R_{rms}), which provides an indicator of surface roughness, revealed changes in surface morphology upon the growth of TiO_2 nanostructures on the membrane. These changes depended on the amount of DEG used as a control agent for the structure. The R_{rms} value of the bare alumina support ranged from 13.0 to 27.5 nm, indicating the macroporous morphology of the support. The TiO_2 nanostructure synthesized with the highest amount of DEG showed slightly reduced R_{rms} values, ranging from 13.5 to 23.7 nm (T1). However, the formation of more TiO_2 nanostructures on the support resulted in increased R_{rms} values for T2 (21.8–32.6 nm) and T3 (24.3–31.4 nm). The changes in the membrane surface were consistent with the SEM surface images shown in Figure 2, and this resulted from an increased surface coverage by larger amounts of TiO_2 nanostructure on the membranes.

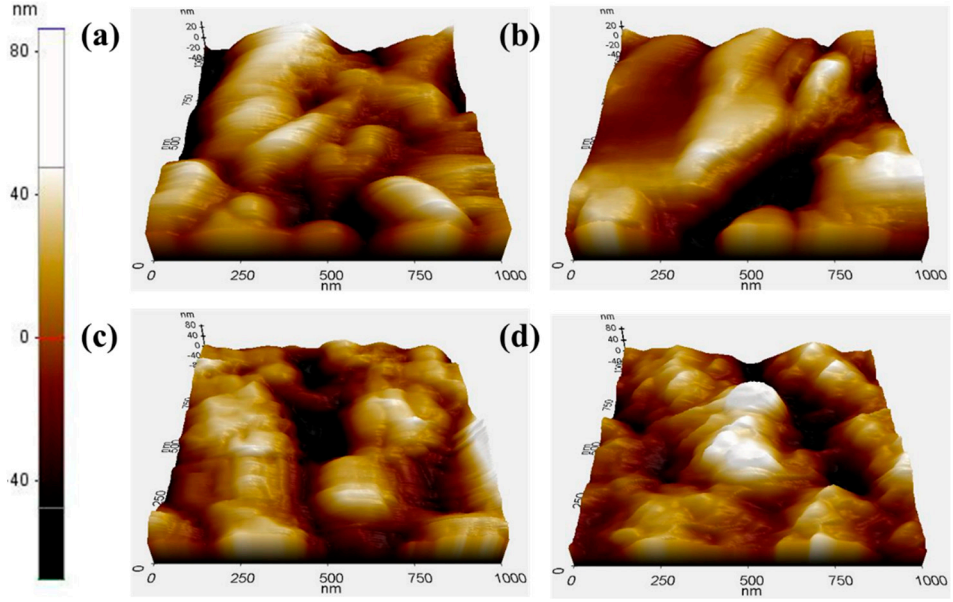

Figure 7. AFM images of the (**a**) bare alumina support, (**b**) T1, (**c**) T2, and (**d**) T3.

3.2. Intrinstic Properties of Membranes

Table 1 compares the overall porosities, membrane thickness, and pure water permeability of the bare alumina support and each TiO_2 on the alumina support, termed the T-series membranes. The porosity (%) of the bare alumina support was 52%, but this reduced to 49%, 49% and 48% for the T1, T2, and T3 membranes, respectively. The thicknesses of all T-series membranes were higher than that of the bare alumina support, owing to the formation of the TiO_2 layer on the support.

The pure water permeability of the alumina support was 44.3 L m^{-2} h^{-1} bar^{-1}, but it decreased to 33.4, 37.7 and 8.3 L m^{-2} h^{-1} bar^{-1} for the T1, T2, and T3 membranes, respectively. The formation of a TiO_2 layer on the support should contribute to resistance against water flow through the membrane [25,28,39]. For the T3 membrane, the pure water flux decreased significantly compared with the other two ceramic membranes. As shown in the SEM images of the T3 membrane (Figure 2), the TiO_2 layer grown on the support had an aggregated structure with shorter and thicker layered clusters compared with those observed for T1 and T2.

Table 1. Properties of bare alumina support and T-series membranes on the support.

Membrane	Porosity (%)	Thickness (cm)	Permeability (L m^{-2} h^{-1} bar^{-1})
T1	49	0.219	33.4
T2	49	0.221	37.7
T3	48	0.225	8.3
Bare	52	0.208	44.3

3.3. Static Adsorption Tests, Photodegradation and Self-Cleaning

Figure 8a shows the results of static adsorption tests performed using the T-series membranes. The ceramic membranes were submerged in a reservoir containing Congo Red dye solution under magnetic stirring for 3 h. For the T1 membrane, 11.5% of the Congo Red dye was adsorbed onto the membrane. The adsorption efficiencies were 5.5% and 9.6% for the T2 and T3 membranes, respectively. The direct growth of TiO_2 nanorod structures on the alumina support may provide a higher surface area for the adsorption sites, as demonstrated by the SEM image in Figure 2c,d [10]. As shown in Figure 2e–h, a less porous structure associated with an aggregated TiO_2 layer on the support was formed on the T2 and T3 membranes, leading to reduced membrane adsorption capacity. As shown in Figure 4b, the TiO_2 nanorod structure was formed uniformly on the alumina support across the

T1 membrane. In addition, complementary cavities and rebinding sites present on the T1 membrane would have provided more adsorption sites for organic dye compounds [40].

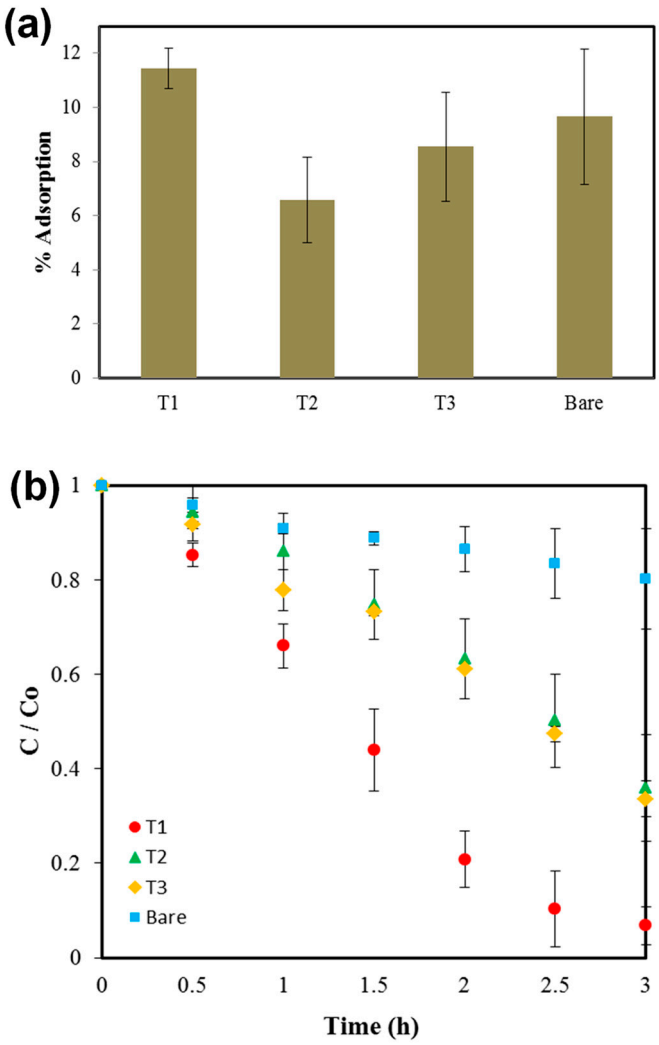

Figure 8. (**a**) The comparison of the percentage of initial concentration of Congo Red dye adsorbed on the surface of the bare alumina support and T-series membranes; (**b**) photocatalytic degradation of Congo Red dye for pre-adsorbed membranes.

After performing static adsorption tests, each membrane was placed in a jacketed beaker containing 50 mL of Congo Red under UV irradiation. Bulk samples were taken at regular time intervals to investigate the UV removal efficiency. With the bare alumina support, an organic removal efficiency of about 20% was obtained after 3 h UV illumination. However, the removal efficiency increased considerably to 93.5%, 64%, and 66.4% for the T1, T2, and T3 membranes, respectively. Indeed, the highest organic removal efficiency was observed with the T1 membrane, consistent with this membrane having the highest adsorption capacity, as shown in Figure 8a. Table 2 compares the photocatalytic degradation efficiency of different organic dye compounds using the photocatalytic membrane. The results, for the photocatalytic degradation of Congo Red with T-series membranes, were further analyzed using pseudo-first-order kinetics, as below:

$$\ln\left(\frac{C}{C_0}\right) = -k_{ap}\, t \tag{3}$$

where C_0 is the initial concentration of Congo Red dye (mg L^{-1}), C is the concentration of dye at a specific time (mg L^{-1}), k_{ap} is the global rate constant (min^{-1}), and t is time (min). From the log-log plots of Equation (3), the rate constants were obtained. The rate constants were measured as 0.82, 0.28, and 0.3 min^{-1} for the T1, T2, and T3 membranes, respectively. Visual observations of digital images of each membrane surface after membrane filtration are compared in Figure 9. Without UV irradiation, severe fouling with a black/red color was observed on each T-series membrane. The UV irradiation of the membranes eliminated the fouling layer; this effect was more pronounced for the T1 membrane than for T2 or T3 membrane.

Table 2. Comparison of dye degradation with other studies.

Photocatalyst	Degradation/Color Removal Efficiency (%)	Dye/Concentration (ppm)	UV/Solar Lamp Wattage (W)	Degradation Time (min)	Reference
Immobilized TNR	52	Reactive Black 5/(10)	36	360	[41]
Immobilized TNR	82	Methyl Orange/(15)	36	100	[42]
Immobilized TiO_2 NPs	42	Reactive Black 5/(40)	15	120	[43]
Immobilized nitrogen-doped graphene/TiO_2	80.6	Methylene Blue/(50)	125	120	[44]
Immobilized α-Fe_2O_3 NR in presence of 75ml/L H_2O_2	88	Congo Red/(20)	150	120	[45]
Immobilized TNR	93.5	Congo Red/(5)	300	180	This study

NPs: Nanoparticles; NR: Nanorods; TiO_2: Titanium dioxide; TNR: TiO_2 nanorod; UV: Ultraviolet; α-Fe_2O_3: Iron oxide.

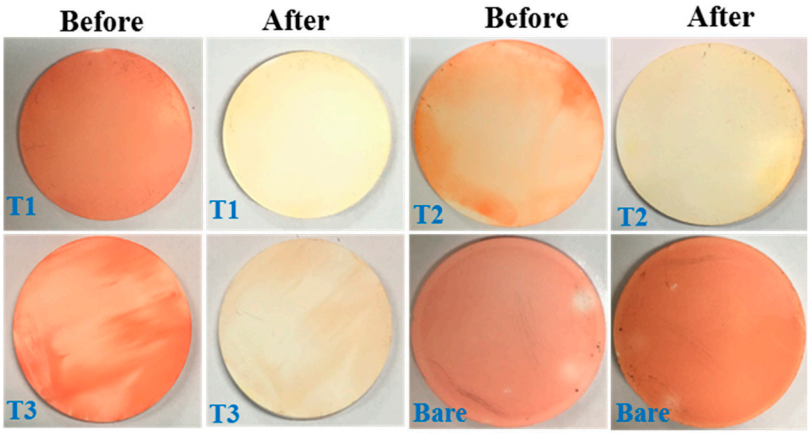

Figure 9. Digital photographs of the bare alumina support and T-series membranes before (i.e., pre-adsorbed membrane) and after (i.e., UV illumination for 3 h) to demonstrate the self-cleaning properties of membranes.

3.4. Antifouling Property by Membrane Fouling Test

The morphological and crystalline structure of a ceramic membrane, rather than the amount of TiO_2 photocatalyst grown on the Al_2O_3 substrate, is the key to improving the antifouling property. Figure 10 shows the change in normalized flux with time during the on-off UV illumination experiments. For the control Al_2O_3 substrate, flux decline was greatest without UV irradiation. When UV irradiation was initiated, the permeate flux started to recover, reaching about 24% of its initial value. With the T1 membrane, the UV irradiation resulted in almost a full recovery of the permeate flux within only 1 h. The complementary cavities and homogenous TiO_2 nanorod structures formed on the Al_2O_3 substrate were thought to allow greater accessibility of the UV light onto the membrane surface and into the pore walls. Both surface and in-pore reactivity associated with the T1 membrane controlled

the organic removal efficiency under UV irradiation [46]. The surface and cross-sectional views of the T1 membrane obtained by SEM (shown in Figures 2 and 4) confirmed the growth of a TiO_2 structure associated with the anatase crystalline phase, both on the membrane surface and in membrane pore walls. Although EDS analysis (Figures 3 and 5) indicated that a smaller amount of TiO_2 was grown on the T1 membrane than on T2 or T3, the permeability of the T1 membrane was much higher than those of the other two membranes under UV illumination. Although the photocatalytic degradation between T2 and T3 membrane was not significantly different as observed in batch study (Figure 8), the layered morphology of the T3 membrane posed detrimental effect not only on membrane antifouling property but also on membrane permeability.

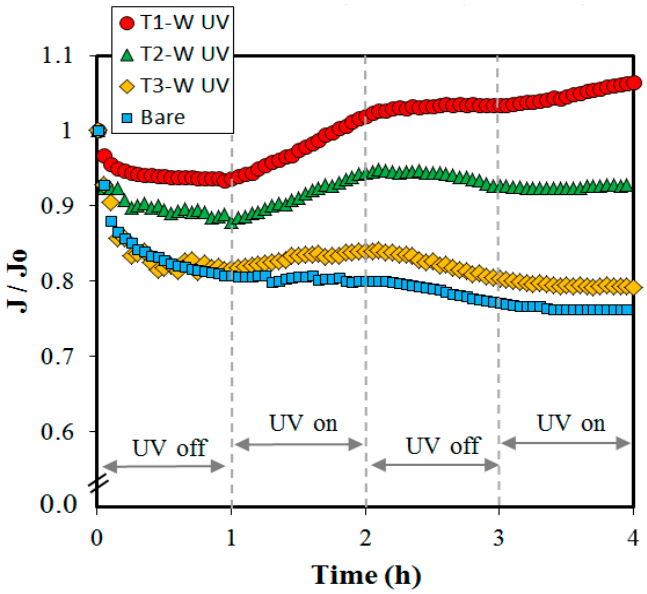

Figure 10. Transient behavior of membrane flux decline during the filtration of Congo Red dye (10 mg L^{-1}) under intermittent UV illumination in photocatalytic membrane reactor (J is instantaneous permeate flux, J_0 is initial permeate flux).

4. Discussion

Figure 11a,b show conceptual diagrams to illustrate the importance of the morphology of catalytic nanomaterials on the inorganic substrate with respect to the performance of a photocatalytic ceramic membrane. The agglomerate structure of TiO_2 formed on the T2 and T3 membranes reduced the accessibility of UV light onto the membrane surface and pore walls, where photocatalytic reactions occur. However, the T1 membrane, with its homogeneous distribution of anatase TiO_2 nanorods, facilitated the catalytic properties of the ceramic membrane. Although co-existence of the anatase and rutile phase of TiO_2 can improve photocatalytic activity for removal of organic materials, it is also known that the combination between them such as composition and morphology should be of great importance for the enhancement of photocatalysis. In other words, the mere co-existence does not necessarily improve photocatalysis, but rather deteriorates it. In the XRD results (Figure 6), the rutile phase with a very low intensity was observed in comparison to the anatase phase with high intensity, indicating the formation of a very small amount of the rutile phase. Therefore, it was regarded that the presence of a small amount of the rutile phase did not enhance the photocatalysis, but rather deteriorated it in this study. As can also be seen in Figure 10, the permeate flux of the T1 membrane in the fouling system was 6% higher than that of the non-fouling system (deionized water only) under UV irradiation. Photo-induced hydrophilicity and the photo-wetting phenomenon caused by UV irradiation appeared to affect membrane permeability [47,48]. A conceptual schematic for better understanding the self-cleaning efficiency of the photocatalytic membrane is also presented in Figure 12. The increase in membrane permeability was mainly due to the photo-reduction of Ti^{4+}

sites to Ti^{3+}, where dissociative water adsorption occurred and hydroxyl groups were readily formed. As a result, the organic foulants at the membrane surface and pore walls were degraded easily, owing to both the surface and in-pore reactivity of the photocatalytic TiO_2 membrane.

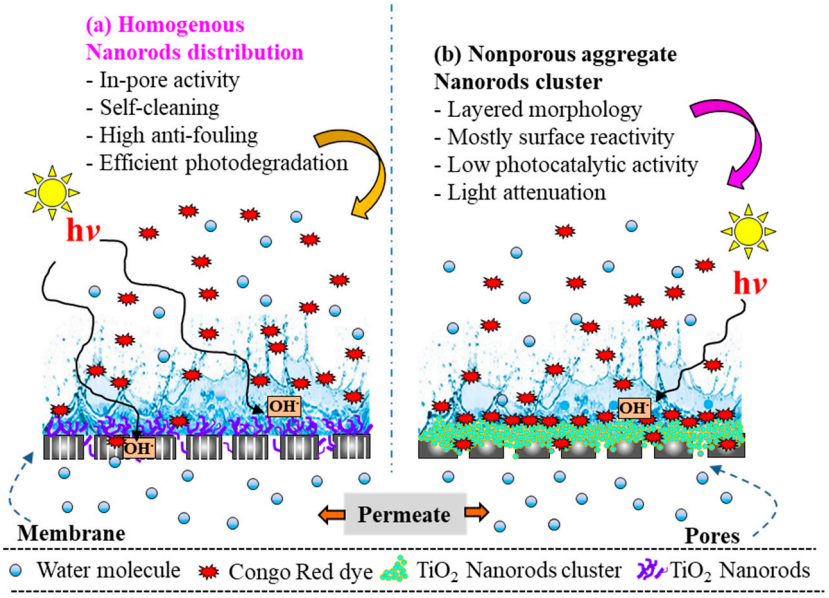

Figure 11. Schematic illustration to demonstrate the performance of the membrane: (**a**) T1 membrane with homogenous distribution of nanorods; and (**b**) T2/T3 membrane with nanorods cluster or aggregates.

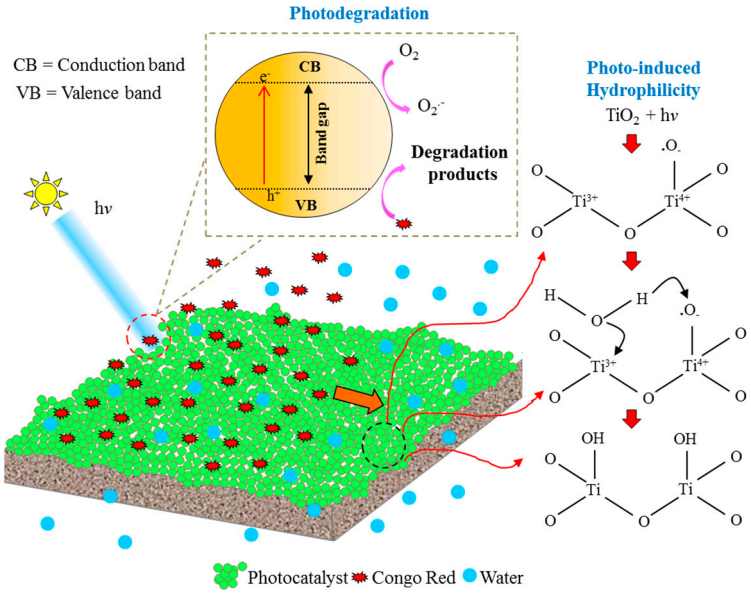

Figure 12. Conceptual schematic illustration of photodegradation and photo-induced hydrophilicity for the T1 membrane.

5. Conclusions

The high-performance photocatalytic membrane was developed by applying DEG-assisted TiO_2 nanostructure on the support. The membranes demonstrated excellent performance, with improved antifouling and organic removal efficiency. Anatase TiO_2 nanorods grown directly on the support were found to be more evenly distributed, not only on the membrane surface but also within membrane pore walls, as the amount of DEG used as a capping agent increased. The well-organized TiO_2 morphology

reduced the perturbation of support, thereby improving the reactivity of the photocatalytic TiO_2 membrane. The highest organic removal efficiency of the Congo Red dye was observed with the T1 membrane consisting of the pure anatase phase of TiO_2 on the membrane support under UV illumination. However, lower DEG concentrations resulted in a non-porous, aggregated TiO_2 layered structure, leading to significantly reduced the reactivity of the photocatalytic membrane. The photocatalytic ceramic membranes fabricated with a homogenous distribution of nanostructures have a profound potential to be applied as next generation membranes in the wastewater treatment industry.

Author Contributions: J.H.K. and J.K. developed and conceived experimental plans and supervised the research methodology and analysis; R.A. and J.K.K. conducted experimental works on development characterizations of photocatalytic membranes and evaluating their performances.

Funding: This research was supported by the National Research Foundation (NRF) of South Korea funded by the Ministry of Science and ICT, Republic of Korea (NRF-2017R1D1A1B06028030). This subject is supported by the Korean Ministry of Environment (MOE) as "Advanced Technology Program for Environmental Industry" (Technologies for the Risk Assessment and Management 20170001400008).

Conflicts of Interest: The authors declare no conflicts of interest.

References

1. Liu, L.; Zheng, G.; Yang, F. Adsorptive removal and oxidation of organic pollutants from water using a novel membrane. *Chem. Eng. J.* **2010**, *156*, 553–556. [CrossRef]
2. Gao, Y.; Hu, M.; Mi, B. Membrane surface modification with TiO_2–graphene oxide for enhanced photocatalytic performance. *J. Membr. Sci.* **2014**, *455*, 349–356. [CrossRef]
3. Zhang, D.; Wang, G.; Zhi, S.; Xu, K.; Zhu, L.; Li, W.; Zeng, Z.; Xue, Q. Superhydrophilicity and underwater superoleophobicity TiO_2/Al_2O_3 composite membrane with ultra low oil adhesion for highly efficient oil-in-water emulsions separation. *Appl. Surf. Sci.* **2018**, *458*, 157–165. [CrossRef]
4. Tabriz, A.; Alvi, M.A.U.R.; Niazi, M.B.K.; Batool, M.; Bhatti, M.F.; Khan, A.L.; Khan, A.U.; Jamil, T.; Ahmad, N.M. Quaternized trimethyl functionalized chitosan based antifungal membranes for drinking water treatment. *Carbohydr. Polym.* **2019**, *207*, 17–25. [CrossRef] [PubMed]
5. Wang, X.; Davies, S.H.; Masten, S.J. Analysis of energy costs for catalytic ozone membrane filtration. *Sep. Purif. Technol.* **2017**, *186*, 182–187. [CrossRef]
6. Zhu, R.; Diaz, A.J.; Shen, Y.; Qi, F.; Chang, X.; Durkin, D.P.; Sun, Y.; Solares, S.D.; Shuai, D. Mechanism of Humic Acid Fouling in a Photocatalytic Membrane System. *J. Membr. Sci.* **2018**. [CrossRef]
7. Lin, Y.-F.; Tung, K.-L.; Tzeng, Y.-S.; Chen, J.-H.; Chang, K.-S. Rapid atmospheric plasma spray coating preparation and photocatalytic activity of macroporous titania nanocrystalline membranes. *J. Membr. Sci.* **2012**, *389*, 83–90. [CrossRef]
8. Ai, J.; Yang, L.; Liao, G.; Xia, H.; Xiao, F. Applications of graphene oxide blended poly(vinylidene fluoride) membranes for the treatment of organic matters and its membrane fouling investigation. *Appl. Surf. Sci.* **2018**, *455*, 502–512. [CrossRef]
9. Kazemi, M.; Jahanshahi, M.; Peyravi, M. Hexavalent chromium removal by multilayer membrane assisted by photocatalytic couple nanoparticle from both permeate and retentate. *J. Hazard. Mater.* **2018**, *344*, 12–22. [CrossRef]
10. Hatat-Fraile, M.; Liang, R.; Arlos, M.J.; He, R.X.; Peng, P.; Servos, M.R.; Zhou, Y.N. Concurrent photocatalytic and filtration processes using doped TiO_2 coated quartz fiber membranes in a photocatalytic membrane reactor. *Chem. Eng. J.* **2017**, *330*, 531–540. [CrossRef]
11. Najma, B.; Kasi, A.K.; Khan Kasi, J.; Akbar, A.; Bokhari, S.M.A.; Stroe, I.R.C. ZnO/AAO photocatalytic membranes for efficient water disinfection: Synthesis, characterization and antibacterial assay. *Appl. Surf. Sci.* **2018**, *448*, 104–114. [CrossRef]
12. Ahmad, R.; Aslam, M.; Park, E.; Chang, S.; Kwon, D.; Kim, J. Submerged low-cost pyrophyllite ceramic membrane filtration combined with GAC as fluidized particles for industrial wastewater treatment. *Chemosphere* **2018**, *206*, 784–792. [CrossRef] [PubMed]
13. Ahmad, R.; Kim, J.; Kim, J.; Kim, J. In-situ TiO_2 formation and performance on ceramic membranes in photocatalytic membrane reactor. *Membr. J.* **2017**, *27*, 328–335. [CrossRef]

14. Ferreiro, C.; Villota, N.; Lombraña, J.I.; Rivero, M.J.; Zúñiga, V.; Rituerto, J.M. Analysis of a Hybrid Suspended-Supported Photocatalytic Reactor for the Treatment of Wastewater Containing Benzothiazole and Aniline. *Water* **2019**, *11*, 337. [CrossRef]
15. Ahmad, R.; Ahmad, Z.; Khan, A.U.; Mastoi, N.R.; Aslam, M.; Kim, J. Photocatalytic systems as an advanced environmental remediation: Recent developments, limitations and new avenues for applications. *J. Environ. Chem. Eng.* **2016**, *4*, 4143–4164. [CrossRef]
16. Karnik, B.S.; Davies, S.H.; Baumann, M.J.; Masten, S.J. Fabrication of catalytic membranes for the treatment of drinking water using combined ozonation and ultrafiltration. *Environ. Sci. Technol.* **2005**, *39*, 7656–7661. [CrossRef]
17. Aoudjit, L.; Martins, P.M.; Madjene, F.; Petrovykh, D.; Lanceros-Mendez, S. Photocatalytic reusable membranes for the effective degradation of tartrazine with a solar photoreactor. *J. Hazard. Mater.* **2018**, *344*, 408–416. [CrossRef] [PubMed]
18. Mendret, J.; Hatat-Fraile, M.; Rivallin, M.; Brosillon, S. Hydrophilic composite membranes for simultaneous separation and photocatalytic degradation of organic pollutants. *Sep. Purif. Technol.* **2013**, *111*, 9–19. [CrossRef]
19. Mondal, K.; Kumar, J.; Sharma, A. TiO_2-nanoparticles-impregnated photocatalytic macroporous carbon films by spin coating. *Nanomater. Energy* **2013**, *2*, 121–133. [CrossRef]
20. Grčić, I.; Papić, S.; Brnardić, I. Photocatalytic activity of TiO_2 thin films: Kinetic and efficiency study. *Int. J. Chem. React. Eng.* **2017**, *16*. [CrossRef]
21. Sanabria Arenas, B.; Strini, A.; Schiavi, L.; Li Bassi, A.; Russo, V.; Del Curto, B.; Diamanti, M.; Pedeferri, M. Photocatalytic Activity of Nanotubular TiO_2 Films Obtained by Anodic Oxidation: A Comparison in Gas and Liquid Phase. *Materials* **2018**, *11*, 488. [CrossRef] [PubMed]
22. Cámara, R.; Portela, R.; Gutierrez-Martin, F.; Sánchez, B. Photocatalytic activity of TiO_2 films prepared by surfactant-mediated sol–gel methods over commercial polymer substrates. *Chem. Eng. J.* **2016**, *283*, 535–543. [CrossRef]
23. Goei, R.; Lim, T.-T. Asymmetric TiO_2 hybrid photocatalytic ceramic membrane with porosity gradient: Effect of structure directing agent on the resulting membranes architecture and performances. *Ceram. Int.* **2014**, *40*, 6747–6757. [CrossRef]
24. Pan, J.H.; Zhao, X.; Lee, W.I. Block copolymer-templated synthesis of highly organized mesoporous TiO_2-based films and their photoelectrochemical applications. *Chem. Eng. J.* **2011**, *170*, 363–380. [CrossRef]
25. Ahmad, R.; Kim, J.K.; Kim, J.H.; Kim, J. Well-organized, mesoporous nanocrystalline TiO_2 on alumina membranes with hierarchical architecture: Antifouling and photocatalytic activities. *Catal. Today* **2017**, *282*, 2–12. [CrossRef]
26. Cao, X.P.; Li, D.; Jing, W.H.; Xing, W.H.; Fan, Y.Q. Synthesis of visible-light responsive C, N and Ce co-doped TiO_2 mesoporous membranes via weak alkaline sol–gel process. *J. Mater. Chem.* **2012**, *22*, 15309–15315. [CrossRef]
27. Ahmad, R.; Kim, J.K.; Kim, J.H.; Kim, J. Effect of polymer template on structure and membrane fouling of TiO_2/Al_2O_3 composite membranes for wastewater treatment. *J. Ind. Eng. Chem.* **2018**, *57*, 55–63. [CrossRef]
28. Alem, A.; Sarpoolaky, H.; Keshmiri, M. Titania ultrafiltration membrane: Preparation, characterization and photocatalytic activity. *J. Eur. Ceram. Soc.* **2009**, *29*, 629–635. [CrossRef]
29. Zhang, S.; Du, Y.; Jiang, H.; Liu, Y.; Chen, R. Controlled synthesis of TiO_2 nanorod arrays immobilized on ceramic membranes with enhanced photocatalytic performance. *Ceram. Int.* **2017**, *43*, 7261–7270. [CrossRef]
30. Zinadini, S.; Zinatizadeh, A.A.; Rahimi, M.; Vatanpour, V.; Zangeneh, H. Preparation of a novel antifouling mixed matrix PES membrane by embedding graphene oxide nanoplates. *J. Membr. Sci.* **2014**, *453*, 292–301. [CrossRef]
31. Cozzoli, P.D.; Kornowski, A.; Weller, H. Low-temperature synthesis of soluble and processable organic-capped anatase TiO_2 nanorods. *J. Am. Chem. Soc.* **2003**, *125*, 14539–14548. [CrossRef]
32. Zhang, Z.; Zhong, X.; Liu, S.; Li, D.; Han, M. Aminolysis route to monodisperse titania nanorods with tunable aspect ratio. *Angew. Chem. Int. Ed.* **2005**, *44*, 3466–3470. [CrossRef]
33. Roh, D.K.; Chi, W.S.; Ahn, S.H.; Jeon, H.; Kim, J.H. One-step Synthesis of Vertically Aligned Anatase Thornbush-like TiO_2 Nanowire Arrays on Transparent Conducting Oxides for Solid-State Dye-Sensitized Solar Cells. *ChemSusChem* **2013**, *6*, 1384–1391. [CrossRef]

34. Roh, D.K.; Chi, W.S.; Jeon, H.; Kim, S.J.; Kim, J.H. High efficiency solid-state dye-sensitized solar cells assembled with hierarchical anatase pine tree-like TiO_2 nanotubes. *Adv. Funct. Mater.* **2014**, *24*, 379–386. [CrossRef]
35. Niu, F.; Zhang, L.-S.; Chen, C.-Q.; Li, W.; Li, L.; Song, W.-G.; Jiang, L. Hydrophilic TiO_2 porous spheres anchored on hydrophobic polypropylene membrane for wettability induced high photodegrading activities. *Nanoscale* **2010**, *2*, 1480–1484. [CrossRef]
36. Qin, A.; Li, X.; Zhao, X.; Liu, D.; He, C. Engineering a highly hydrophilic PVDF membrane via binding TiO_2 nanoparticles and a PVA layer onto a membrane surface. *ACS Appl. Mater. Interfaces* **2015**, *7*, 8427–8436. [CrossRef]
37. Ozawa, K.; Yamamoto, S.; Yukawa, R.; Liu, R.-Y.; Terashima, N.; Natsui, Y.; Kato, H.; Mase, K.; Matsuda, I. Correlation between Photocatalytic Activity and Carrier Lifetime: Acetic Acid on Single-Crystal Surfaces of Anatase and Rutile TiO_2. *J. Phys. Chem. C* **2018**, *122*, 9562–9569. [CrossRef]
38. Pigeot-Rémy, S.; Dufour, F.; Herissan, A.; Ruaux, V.; Maugé, F.; Hazime, R.; Foronato, C.; Guillard, C.; Chaneac, C.; Durupthy, O. Bipyramidal anatase TiO_2 nanoparticles, a highly efficient photocatalyst? Towards a better understanding of the reactivity. *Appl. Catal. B Environ.* **2017**, *203*, 324–334. [CrossRef]
39. Ahmad, R.; Kim, J.K.; Kim, J.H.; Kim, J. Nanostructured ceramic photocatalytic membrane modified with a polymer template for textile wastewater treatment. *Appl. Sci.* **2017**, *7*, 1284. [CrossRef]
40. Zhao, K.; Feng, L.; Lin, H.; Fu, Y.; Lin, B.; Cui, W.; Li, S.; Wei, J. Adsorption and photocatalytic degradation of methyl orange imprinted composite membranes using TiO_2/calcium alginate hydrogel as matrix. *Catal. Today* **2014**, *236*, 127–134. [CrossRef]
41. Mohtor, N.H.; Othman, M.H.D.; Bakar, S.A.; Kurniawan, T.A.; Dzinun, H.; Norddin, M.N.A.M.; Rajis, Z. Synthesis of nanostructured titanium dioxide layer onto kaolin hollow fibre membrane via hydrothermal method for decolourisation of reactive black 5. *Chemosphere* **2018**, *208*, 595–605. [CrossRef]
42. Tao, J.; Gong, Z.; Yao, G.; Cheng, Y.; Zhang, M.; Lv, J.; Shi, S.; He, G.; Chen, X.; Sun, Z. Hydrothermal growth of nanorod arrays and in situ conversion to nanotube arrays for highly efficient Ag-sensitized photocatalyst. *J. Alloys Compd.* **2016**, *689*, 451–459. [CrossRef]
43. You, S.-J.; Semblante, G.U.; Lu, S.-C.; Damodar, R.A.; Wei, T.-C. Evaluation of the antifouling and photocatalytic properties of poly (vinylidene fluoride) plasma-grafted poly (acrylic acid) membrane with self-assembled TiO_2. *J. Hazard. Mater.* **2012**, *237*, 10–19. [CrossRef]
44. Xu, H.; Ding, M.; Chen, W.; Li, Y.; Wang, K. Nitrogen–doped GO/TiO_2 nanocomposite ultrafiltration membranes for improved photocatalytic performance. *Sep. Purif. Technol.* **2018**, *195*, 70–82. [CrossRef]
45. Zhang, E.; Wang, L.; Zhang, B.; Xie, Y.; Sun, C.; Jiang, C.; Zhang, Y.; Wang, G. Modification of polyvinylidene fluoride membrane with different shaped α-Fe_2O_3 nanocrystals for enhanced photocatalytic oxidation performance. *Mater. Chem. Phys.* **2018**, *214*, 41–47. [CrossRef]
46. Horovitz, I.; Avisar, D.; Baker, M.A.; Grilli, R.; Lozzi, L.; Di Camillo, D.; Mamane, H. Carbamazepine degradation using a N-doped TiO_2 coated photocatalytic membrane reactor: Influence of physical parameters. *J. Hazard. Mater.* **2016**, *310*, 98–107. [CrossRef]
47. Lee, H.Y.; Park, Y.H.; Ko, K.H. Correlation between Surface Morphology and Hydrophilic/Hydrophobic Conversion of MOCVD−TiO_2 Films. *Langmuir* **2000**, *16*, 7289–7293. [CrossRef]
48. Moustakas, N.; Katsaros, F.; Kontos, A.; Romanos, G.E.; Dionysiou, D.; Falaras, P. Visible light active TiO_2 photocatalytic filtration membranes with improved permeability and low energy consumption. *Catal. Today* **2014**, *224*, 56–69. [CrossRef]